

Supporting Information for

Molecular Trade-offs between Lattice Oxygen and Oxygen Vacancy Drive Organic Pollutant Degradation in Fungal Biomineralized Exoskeletons

Zhi-Lai Chi,^{1,2} Guang-Hui Yu,^{1,*} H. Henry Teng,^{1,3} Hai-Gang Liu,⁴ Jian Wang,⁵ Cong-Qiang Liu,¹ Qi-Rong Shen,² and Geoffrey Michael Gadd^{6,7}

* Corresponding Author

Phone: +86 22 27405053; fax: +86-22 27405051; email: yuguanghui@tju.edu.cn

Number of text pages: 21;

Number of Figures: 12;

Number of Tables: 3

Supporting Materials and Methods

LC-MS Determination. The liquid chromatography-mass spectrometry (LC-MS) system used an Ultimate 3000 UHPLC-Q-Exactive-MS (Thermo Scientific, US). Ionization conditions were as follows: heated electrospray ionization (HESI), spray voltage: 3.2 kV, cone voltage: 30 V; source block temperature: 120 °C, capillary temperature: 300 °C. Separation was carried out using a waters C18 (100 mm×2.1 mm, 1.7 μm) at 40 °C under isocratic conditions with 0.1% formic acid/AcCN (90:10) mobile phase. The flow rate and injection volume were 0.3 mL/min and 5 μL, respectively. MS analysis (m/z 50-750) was carried out in negative ionization mode.

Fluorescence Determination. Samples were taken at the times intervals 0, 24, 48, and 66 h and filtered through 0.22 μm polytetrafluoroethylene (PTFE) filters. The filtered samples were further diluted to dissolved organic carbon (DOC) <10 mg/L. Fluorescence excitation-emission matrix (EEM) spectra were measured on a Varian eclipse fluorescence spectrophotometer in scan mode. Scanning emission (Em) spectra from 250 to 550 nm were obtained in 2 nm increments by varying the excitation (Ex) wavelength from 200 to 450 nm in 10 nm increments¹. The spectra were recorded at a scan rate of 1200 nm/min, using excitation and emission slit bandwidths of 5 nm. The voltage of the photomultiplier tube (PMT) was set at 800 V for low level light detection. The temperature of the samples was maintained at room temperature (20 °C) during the analyses. Each Excel data of scan was composed of 171 Em (row) × 31 Ex (column) wavelengths.

STXM-NEXAFS Analyses. Stack datasets for STXM-NEXAFS

spectromicroscopy from the section were collected in the transmission mode, with a He atmosphere. For the stacks, a dwell time (DT) of 1 ms was used with slit size 20/20, and a 35 nm outmost-zone zone plate was used for X-ray focusing. The high-resolution stack datasets were read and preprocessed using the Analysis of X-ray Microscopy Images and Spectra software (aXis2000). Image sequences (i.e., stacks) were recorded by changing the monochromator in energy increments varying from 0.15 to 1.5 eV as follows: (i) C K-edge 280.0–283.0 eV in 0.75 eV steps, 283.0–292.0 eV in 0.15 eV steps, 292.1–305.0 eV in 0.5 eV steps, and 305.5–320.0 eV in 1.5 eV steps; (ii) N K-edge 395.0–398.0 eV in 0.75 eV steps, 398.0–405.2 eV in 0.2 eV steps, 405.2–420.0 eV in 0.74 eV steps, and 420.0–435.0 in 1.45 eV steps; (iii) O K-edge 525.0–529.0 eV in 0.80 eV steps, 529.0–535.2 eV in 0.2 eV steps, 535.2–549.497 eV in 0.493 eV steps, and 549.497–560.0 eV in 1.583 eV steps; (iv) Fe L-edge 700.0–706.0 eV in 0.75 eV steps, 706.0–714.2 eV in 0.20 eV steps, 714.2–720.0 eV in 0.725 eV steps, and 720.0–735.0 eV in 0.30 eV steps.

C 1s NEXAFS Spectra. C 1s NEXAFS spectra were collected from BL02B01 at the Shanghai Synchrotron Radiation Facility (SSRF). For sample preparation, one droplet of filtrate was deposited at a 100 nm thickness onto a Cu slice. The C 1s NEXAFS spectra were recorded in the energy from 280 to 310 eV in 0.1 eV steps (dwell time 1 ms). The Gaussian curve component positions were verified by examining the spectra of previously measured standards as representatives of specific functional groups^{2,3}. An arctangent function was used to model the ionization step and was fixed at 290 eV. All the data were normalized before curve fitting using the ATHENA

(version 2.1.1) and Peak Fit software.

Chemical Analyses. For chemical analyses, samples were first filtered through 0.22 μm PTFE filters. The filtrate (10 ml) was used to determine dissolved Fe by inductively coupled plasma-atomic emission spectroscopy (710/715 ICP-AES, Agilent, Australia). The solution pH was determined using a Mettler-Toledo acidimeter. The mycelia were dispersed by ultrasound, washed with Milli-Q water, and collected by filtration through a 0.22 μm PTFE filter, followed by oven-drying (65 $^{\circ}\text{C}$) before being ground into powder. The organic carbon content of the powdered biomass was analyzed using a Vario MACRO cube elemental analyzer (Elementar Inc.) calibrated using a sulfanilamide standard (Elemental Microanalysis, Germany) with 41.81 wt.% carbon.

The concentration of H_2O_2 in the solution was quantified fluorometrically using microtiter plates which allows detection of 5 pmol with 2 μM amplex red (AR) and 1 kU L^{-1} horseradish peroxidase (HRP) as the fluorescence reagent⁴. H_2O_2 in the presence of HRP reacts with Amplex Red with 1:1 stoichiometry to produce fluorescent resorufin which has absorption and fluorescence emission maxima at 563 and 587 nm respectively. Prior to analysis, samples were mixed with 10 mM phosphate buffer (pH 8) to adjust the solution pH to ~ 8.0 ⁵.

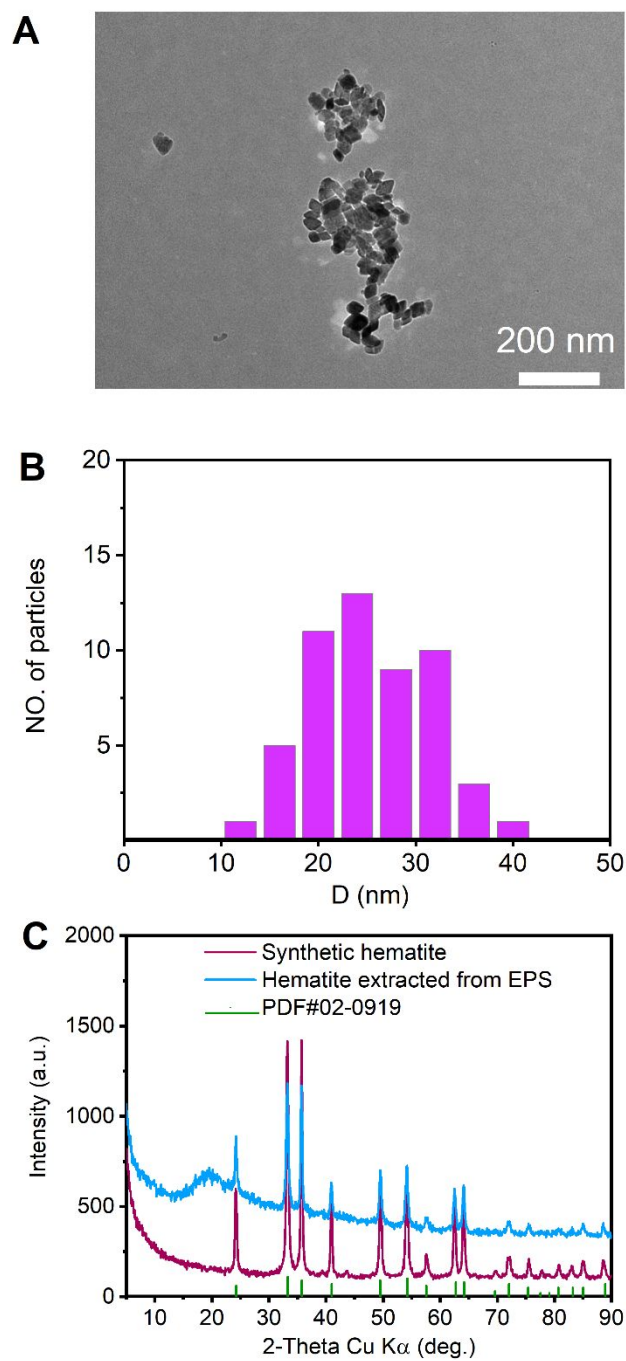


Figure S1. TEM image (A), size-distribution histogram analysis (B), and X-ray powder diffraction (C) of synthetic hematite.

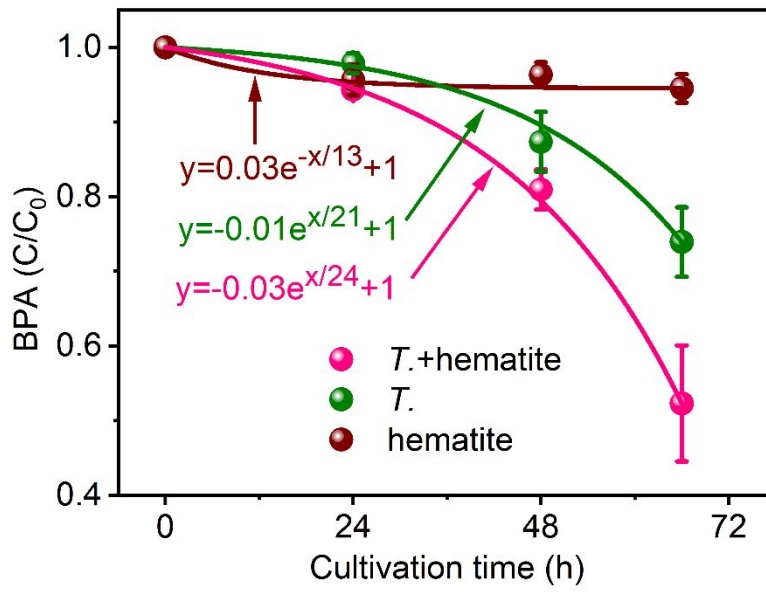


Figure S2. Degradation efficiency of BPA in the different treatments (n = 3).

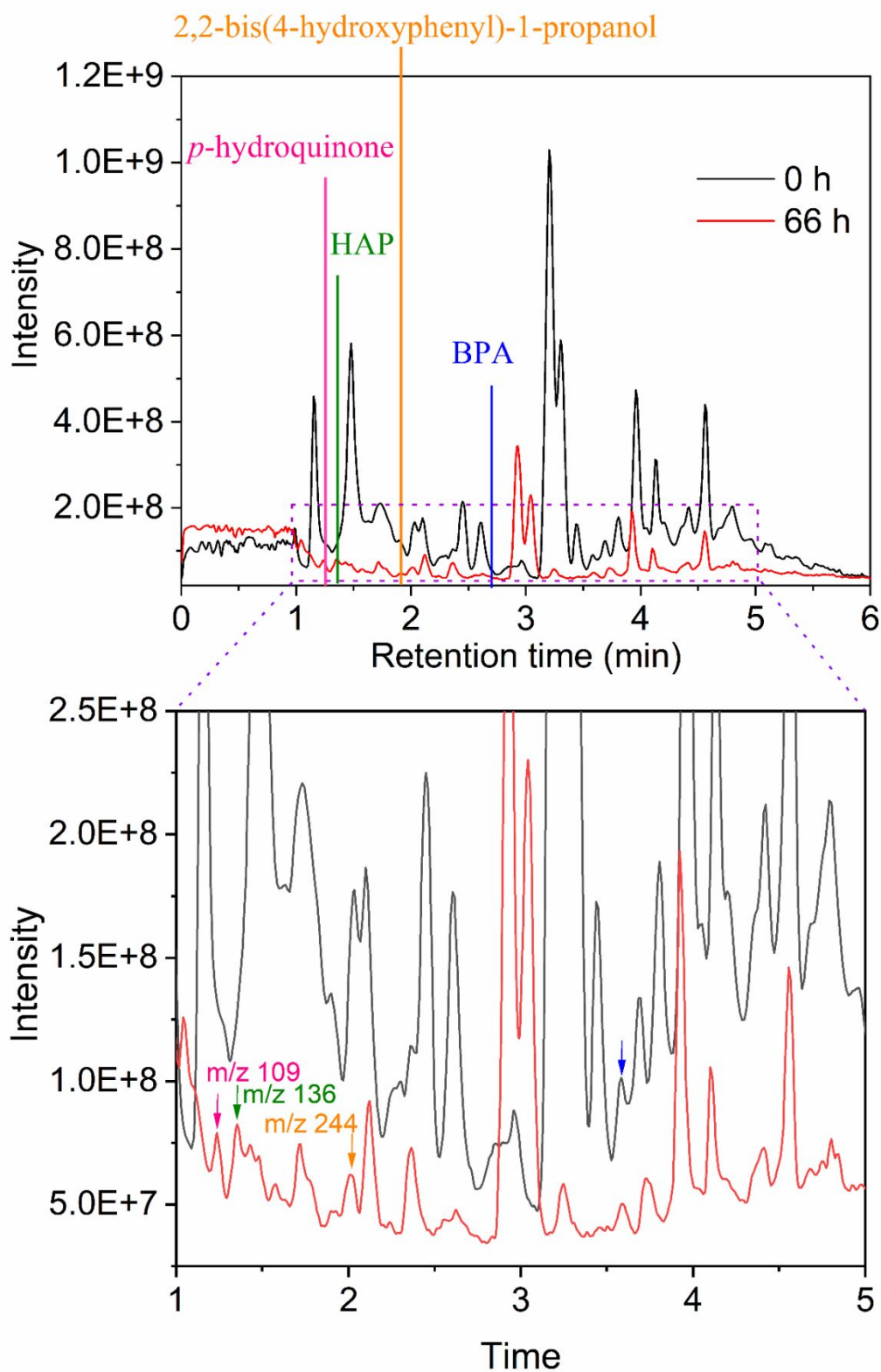


Figure S3. Total ions chromatogram (TIC) from LC-MS during BPA degradation by *T. guizhouense* + hematite in liquid medium. The peaks appearing at 1.23 min, 1.34 min, 1.90 min, and 3.58 min were assigned to *p*-hydroquinone (m/z 109)⁶, 4-

hydroxyacetophenone (HAP) (m/z 136)⁷, 2,2-bis(4-hydroxyphenyl)-1-propanol (m/z 244)⁸, and BPA (m/z 228)^{6,9}, respectively. HAP and *p*-hydroquinone are also frequently found in oxidation of BPA by HO•^{7,10,11}. Subsequently, 2,2-bis(4-hydroxyphenyl)-1-propanol was further metabolized by *T. guizhouense* through cleavage of the C–C bond between the phenolic moiety and the isopropyl group of BPA to form *p*-hydroquinone (HQ). HQ was further degraded into organic acids or completely degraded by microorganisms¹². HAP was also completely metabolized by microorganisms¹².

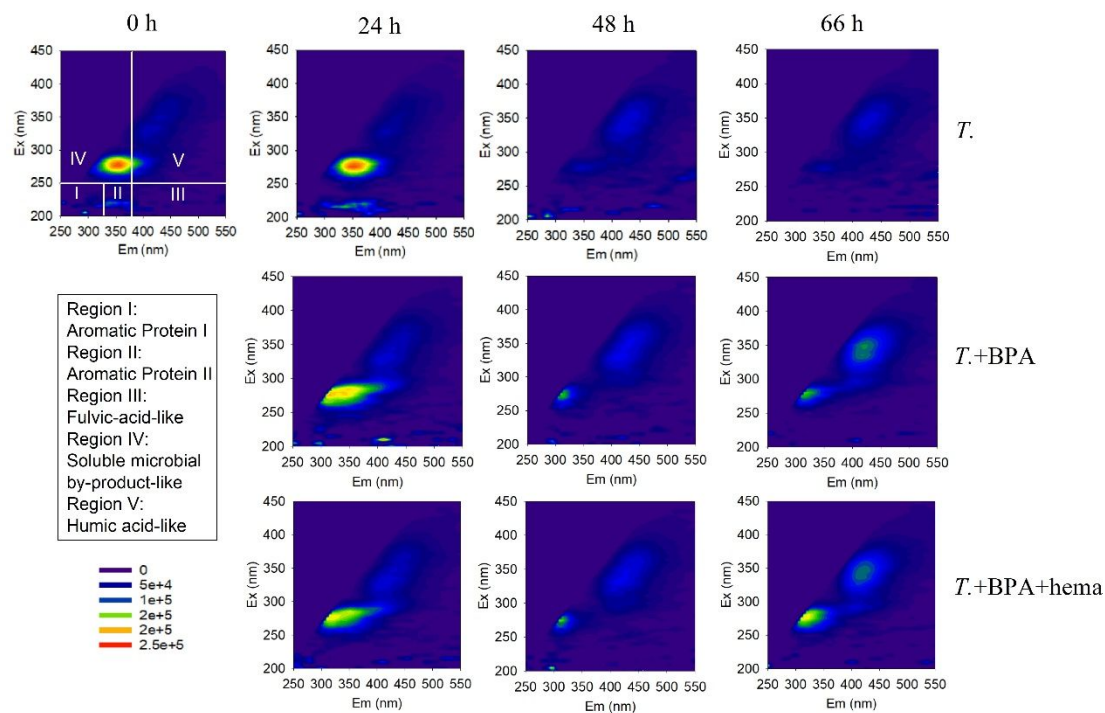


Figure S4. Changes in biological activity of the fungus during growth in the absence or presence of hematite and BPA, as indicated by fluorescence excitation-emission matrix spectroscopy. Fluorophore at the $Ex/Em = 310 \pm 320 \text{ nm}/380 \pm 410 \text{ nm}$ was used to evaluate biological activity¹³. This fluorophore corresponds to fungal-produced humic acid-like substances (Region V)¹⁴.

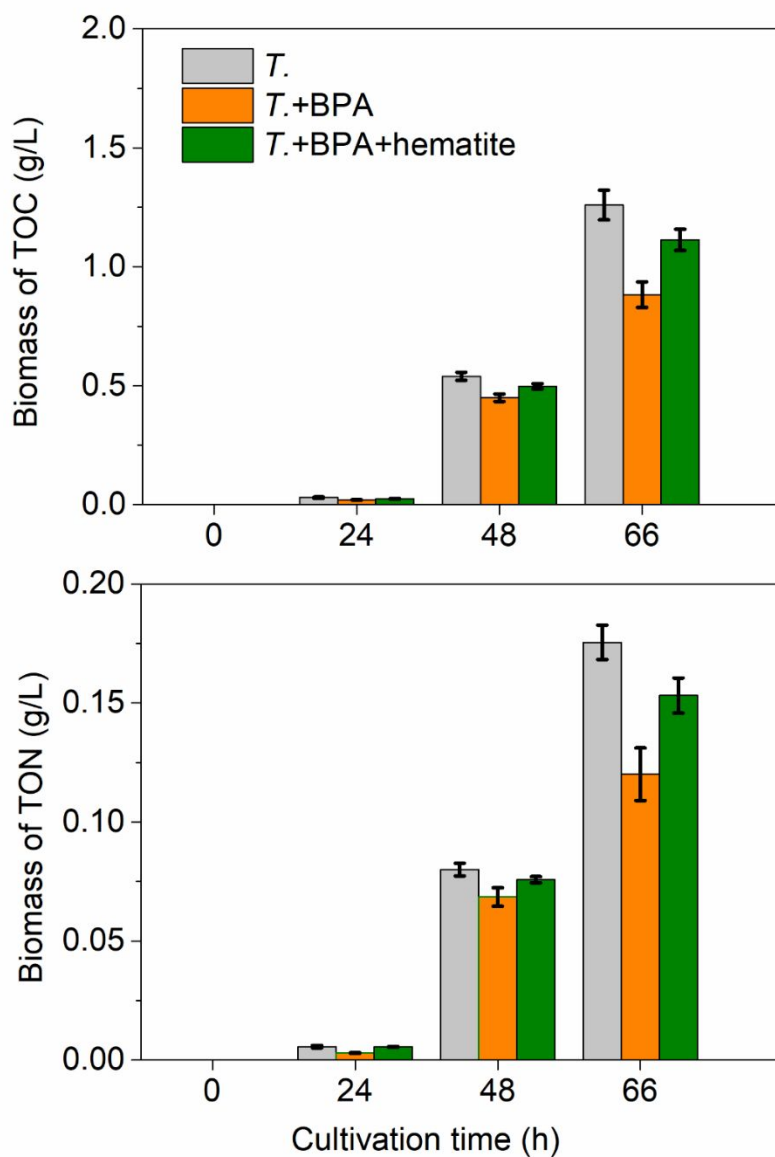


Figure S5. Changes in fungal biomass (based on TOC and TON contents) during growth in the absence or presence of hematite and BPA. TOC, total organic carbon; TON, total organic nitrogen; BPA, bisphenol A. Data are shown as means \pm S.D. (n = 3).

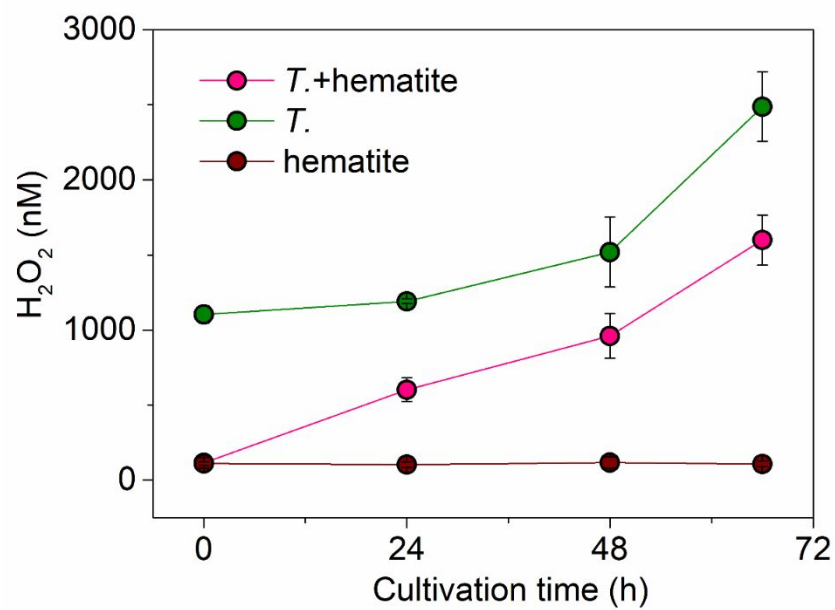


Figure S6. Changes in H₂O₂ concentrations during fungal cultivation. Data are shown as means \pm S.D. (n = 3).

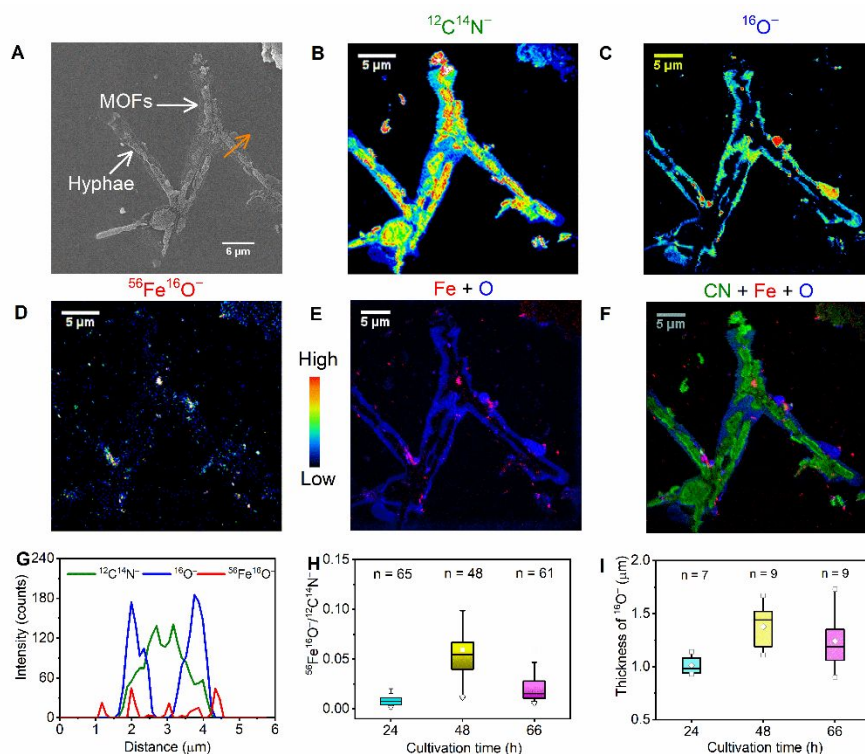


Figure S7. Correlative SEM and NanoSIMS images showing the location of fungal coatings and their development with cultivation time. (A) SEM image showing the clear borderline between fungal hyphae and coatings after 66 h cultivation. (B-D) NanoSIMS images showing the location of biomass ($^{12}\text{C}^{14}\text{N}^-$, (B)), oxygen ($^{16}\text{O}^-$, (C)), and iron oxide ($^{56}\text{Fe}^{16}\text{O}^-$, (D)) after 66 h cultivation. (E) Composite image of $^{56}\text{Fe}^{16}\text{O}^-$ and $^{16}\text{O}^-$. (F) Composite image of $^{12}\text{C}^{14}\text{N}^-$, $^{56}\text{Fe}^{16}\text{O}^-$ and $^{16}\text{O}^-$. (G) Line profile of $^{12}\text{C}^{14}\text{N}^-$, $^{16}\text{O}^-$, and $^{56}\text{Fe}^{16}\text{O}^-$ with a position shown in (A) as orange arrow. (H) Changes in $^{56}\text{Fe}^{16}\text{O}^-/^{12}\text{C}^{14}\text{N}^-$ ratios with cultivation time. (I) Regions of interest (ROI) analysis indicating changes of $^{16}\text{O}^-$ thickness with cultivation time. The lines in the box are the median value in the middle and the mean value as the square. The lines at the edge of the boxes represent the 25th and 75th population percentiles. The “n” in (H) and (I) is the number of ROI and line profiles from NanoSIMS images, respectively.

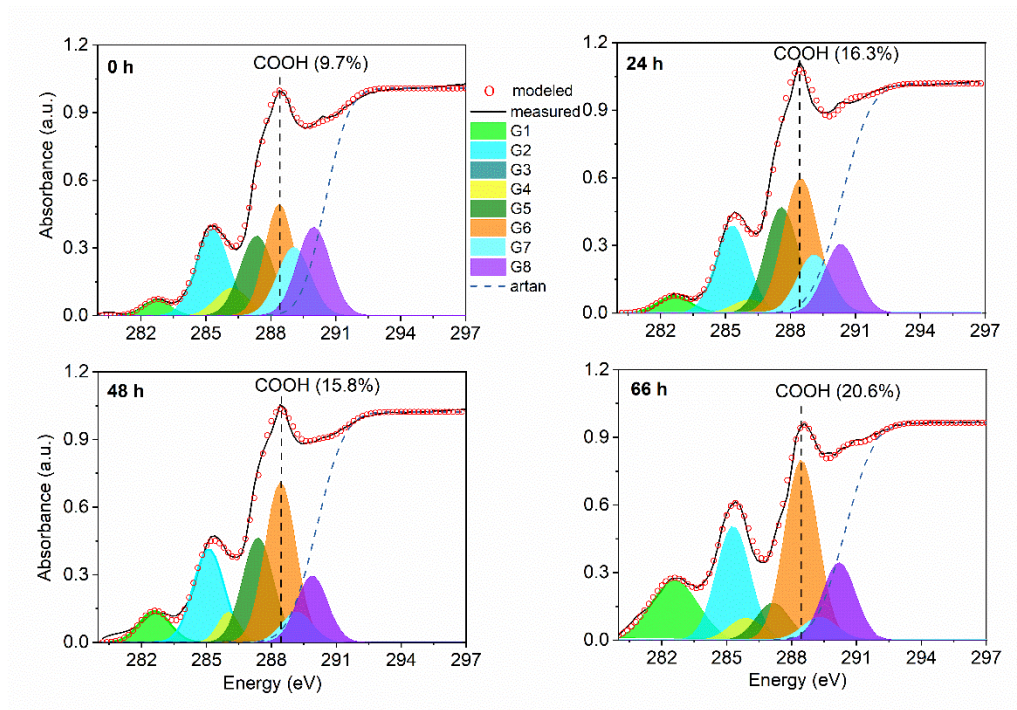


Figure S9. C 1s NEXAFS spectra of fungal-mineral samples after cultivation for 0, 24, 48, and 66 h. Note that G1-G8 represents eight Gaussian curves. Artan represents an arctangent step function. The specific C forms of G1-G8 are given in Table S1. Open circles indicate experimental data and solid lines show the model fits.

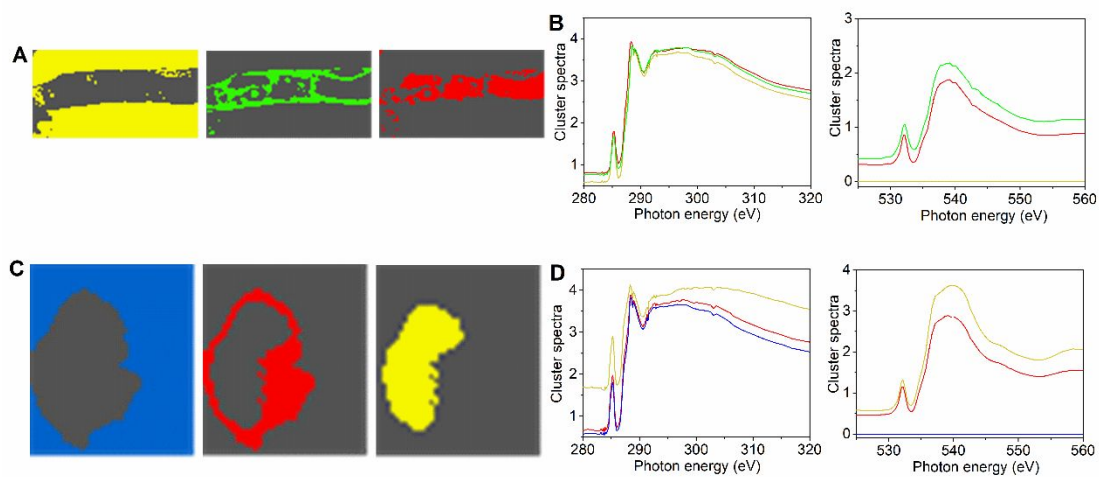


Figure S10. Individual cluster images (A, B) and C 1s and O 1s NEXAFS spectra (C, D) of the transverse and longitudinal cross-section samples in Figure 2(C). (A) and (C), the longitudinal cross-section. (B) and (D), the transverse cross-section.

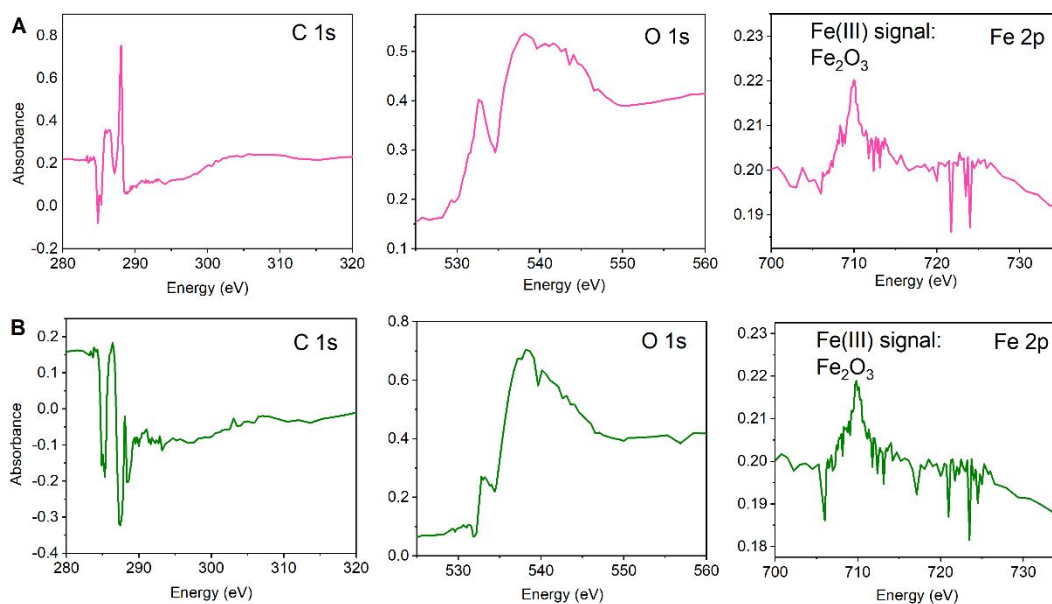


Figure S11. Difference spectra derived from STXM images of the longitudinal cross-section (500 nm-thickness) shown in Figure 2(C). (A) Optical density difference spectra derived from the red region minus the yellow region in Figure 2C up (transverse cross-section) and Figure S10A and S10B at C 1s, O 1s, and Fe 2p, respectively. (B) Optical density difference spectra derived from the green region minus the yellow region in Figure 2C up and Figure S10A and S10B at C 1s, O 1s, and Fe 2p, respectively. Two characteristic peaks were identified at 285.5 eV (C=C 1 $s\text{-}\pi^*$ transition in aromatic carbon) and at 288.6 eV (1 $s\text{-}\pi^*$ transition of amide carbonyl and C-N bonds)^{15,16}.

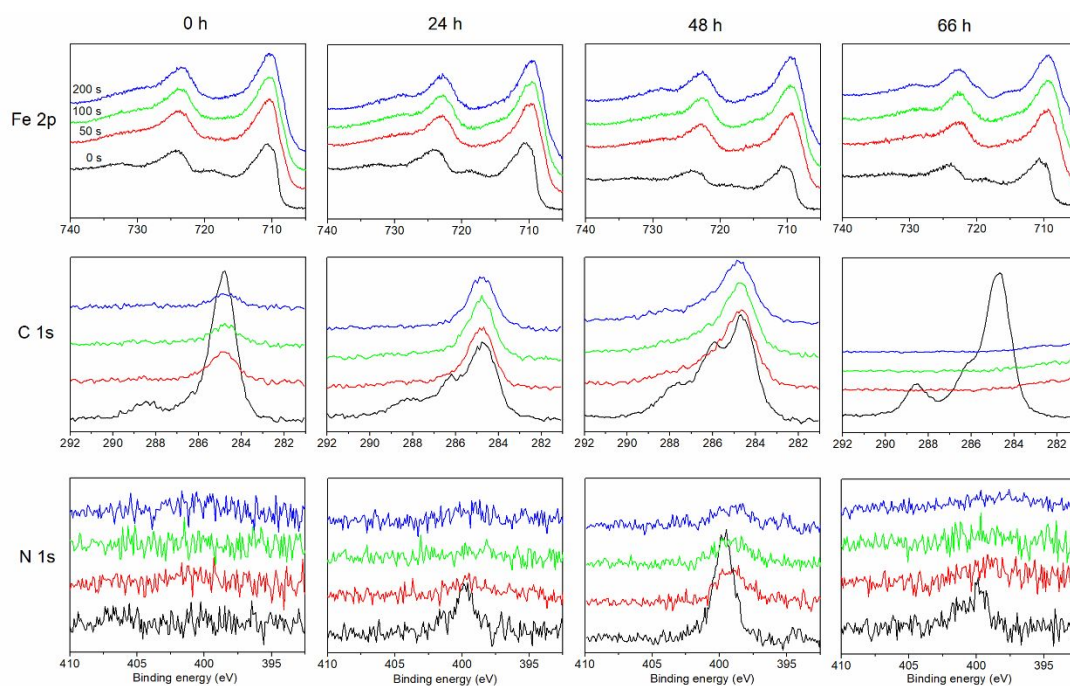


Figure S12. Time-resolved Fe 2p, C 1s and N1s depth profiles of XPS spectra during fungal biomineralization. Etch time was set as 0 s, 50 s, 100 s, and 200 s, which was approximately 0.4 nm/s at the experimental conditions.

Table S1. Peak deconvolution for C 1s NEXAFS spectra of the solution at different cultivation times.

Cultivation time	The proportion of absorption regions (%)					
	Aromatic C	Phenolic C	Alkyl C	Carboxylic C	O-alkyl	Carbonyl C
	283-286.1 eV (G1-G3)	286-287.5 eV G4	287.6-288.3 eV G5	288.4-289.1 eV G6	289.2-289.8 eV G7	289.9-291.2 eV G8
0 h	44.5	11.3	22.3	9.7	9.4	2.8
24 h	23.7	15.0	28.8	16.3	6.9	9.2
48 h	28.0	14.0	26.9	15.8	11.8	3.5
66 h	20.4	13.7	17.6	20.6	14.2	13.5

Table S2. Changes in dissolved Fe and pH during fungal cultivation.

Cultivation time	Dissolved Fe (mg/L)	pH		
		<i>T.</i> + hematite	<i>T.</i>	Hematite
0 h	0.01 ± 0.00	5.65 ± 0.03	5.66 ± 0.03	5.67 ± 0.02
24 h	0.23 ± 0.02	5.41 ± 0.06	5.36 ± 0.05	5.57 ± 0.02
48 h	1.15 ± 0.09	3.24 ± 0.04	3.31 ± 0.06	5.57 ± 0.01
66 h	1.53 ± 0.09	2.33 ± 0.06	2.26 ± 0.09	5.58 ± 0.03

Note: All experiments were conducted in triplicate. Data are means ± standard deviation (n = 3).

Table S3. Changes in the relative percentages of O_L and O_V with cultivation time.

Cultivation time (h)	O_L (%)	O_V (%)
0	85.35	14.83
24	78.79	21.21
48	72.86	27.15
66	68.58	31.42

Note: O_L , lattice oxygen. O_V , oxygen vacancy.

REFERENCES

1. Yu, G.; Wu, M.; Wei, G.; Luo, Y.; Ran, W.; Wang, B.; Zhang, J.; Shen, Q., Binding of organic ligands with Al(III) in dissolved organic matter from soil: implications for soil organic carbon storage. *Environ. Sci. Technol.* **2012**, *46*, (11), 6102–6109.
2. Li, H.; Hu, S.; Polizzotto, M. L.; Chang, X.; Shen, Q.; Ran, W.; Yu, G., Fungal biomineralization of montmorillonite and goethite to short-range-ordered minerals. *Geochim. Cosmochim. Acta* **2016**, *191*, 17–31.
3. Kleber, M.; Nico, P. S.; Plante, A.; Filley, T.; Kramer, M.; Swanston, C.; Sollins, P., Old and stable soil organic matter is not necessarily chemically recalcitrant: Implications for modeling concepts and temperature sensitivity. *Glob. Change Biol.* **2011**, *17*, (2), 1097–1107.
4. Zhou M , D. Z., Panchuk-Voloshina N, Haugland, R. P., A stable nonfluorescent derivative of resorufin for the fluorometric determination of trace hydrogen peroxide: Applications in detecting the activity of phagocyte NADPH oxidase and other oxidases. *Analy. Biochem.* **1997**, *253*, (2), 162–168.
5. Yu, G.-H.; Chi, Z.-L.; Kappler, A.; Sun, F.-S.; Liu, C.-Q.; Teng, H. H.; Gadd, G. M., Fungal nanophase particles catalyze iron transformation for oxidative stress removal and iron acquisition. *Curr. Biol.* **2020**, *30*, (15), 2943–2950.
6. Zhang, C.; Zeng, G.; Yuan, L.; Yu, J.; Li, J.; Huang, G.; Xi, B.; Liu, H., Aerobic degradation of bisphenol A by *Achromobacter xylosoxidans* strain B-16 isolated from compost leachate of municipal solid waste. *Chemosphere* **2007**, *68*, (1), 181–190.
7. Nomiyama, K.; Tanizaki, T.; Koga, T.; Arizono, K.; Shinohara, R., Oxidative degradation of BPA using TiO₂ in water, and transition of estrogenic activity in the degradation pathways. *Arch. Environ. Contam. Toxicol.* **2007**, *52*, (1), 8–15.
8. Sasaki, M.; Akahira, A.; Oshiman, K.; Tsuchido, T.; Matsumura, Y., Purification of cytochrome P450 and ferredoxin, involved in bisphenol A degradation, from *Sphingomonas* sp. strain AO1. *Appl. Environ. Microbiol.* **2005**, *71*, (12), 8024–8030.
9. Sajiki, J.; Hasegawa, Y.; Hashimoto, H.; Makabe, Y.; Miyamoto, F.; Yanagibori, R.; Shin, J.; Shimidzu, Y.; Morigami, T., Determination of bisphenol A (BPA) in plasma of hemodialysis patients using three methods: LC/ECD, LC/MS, and ELISA. *Toxicol. Mechanisms Methods* **2008**, *18*, (9), 733–738.
10. Daâssi, D.; Prieto, A.; Zouari-Mechichi, H.; Martínez, M. J.; Nasri, M.; Mechichi, T., Degradation of bisphenol A by different fungal laccases and identification of its degradation products. *Int. Biodeterior. Biodegradation* **2016**, *110*, 181–188.
11. Subagio, D. P.; Srinivasan, M.; Lim, M.; Lim, T.-T., Photocatalytic degradation of bisphenol-A by nitrogen-doped TiO₂ hollow sphere in a vis-LED photoreactor. *Appl.*

Cataly. B: Environ. **2010**, *95*, (3–4), 414–422.

12. Zhang, W.; Yin, K.; Chen, L., Bacteria-mediated bisphenol A degradation. *Appl. Microbiol. Biotechnol.* **2013**, *97*, (13), 5681–5689.

13. Parlanti, E.; Wörz, K.; Geoffroy, L.; Lamotte, M., Dissolved organic matter fluorescence spectroscopy as a tool to estimate biological activity in a coastal zone submitted to anthropogenic inputs. *Org. Geochem.* **2000**, *31*, (12), 1765–1781.

14. Chen, W.; Westerhoff, P.; Leenheer, J. A.; Booksh, K., Fluorescence excitation–emission matrix regional integration to quantify spectra for dissolved organic matter. *Environ. Sci. Technol.* **2003**, *37*, (24), 5701–5710.

15. Keiluweit, M.; Bougoure, J. J.; Zeglin, L. H.; Myrold, D. D.; Weber, P. K.; Pett-Ridge, J.; Kleber, M.; Nico, P. S., Nano-scale investigation of the association of microbial nitrogen residues with iron (hydr)oxides in a forest soil O-horizon. *Geochim. Cosmochim. Acta* **2012**, *95*, 213–226.

16. Bonneville, S.; Delpomdor, F.; Pr at, A.; Chevalier, C.; Araki, T.; Kazemian, M.; Steele, A.; Schreiber, A.; Wirth, R.; Benning, L. G., Molecular identification of fungi microfossils in a Neoproterozoic shale rock. *Sci. Adv.* **2020**, *6*, (4), eaax7599.